

Simulation of the high temperature impression of thermal barrier coatings with columnar microstructure

Xi Chen ^{a,*}, John W. Hutchinson ^b, Anthony G. Evans ^c

^a Department of Civil Engineering and Engineering Mechanics, Columbia University, 500 West 120th Street, New York, 10027, USA

^b Division of Engineering and Applied Sciences, Harvard University, 29 Oxford Street, Cambridge, MA 02138, USA

^c Materials Department, University of California, Santa Barbara, CA 93106, USA

Received 22 July 2003; received in revised form 24 September 2003; accepted 27 September 2003

Abstract

The phenomena governing the durability of thermal barrier coatings (TBCs) are affected by their high temperature mechanical properties: especially the mechanisms of material removal upon particle impact. Some high temperature properties can be explored using an impression test described in a companion article. The utility of the test is contingent upon a method for deconvoluting aspects of the stress/strain response from load–displacement measurements. A numerical procedure having this attribute is described, and applied to TBCs with a columnar microstructure. The method elucidates the extent of the plastic deformation and densification as well as the column distortions caused by the impression. It is also capable of exploring the deformation heterogeneities observed experimentally, such as shear bands, by embodying salient constituent properties, such as the column width, contact friction, and inter-columnar friction. Comparisons with measurements provide some understanding of the plastic response of several thermal barrier systems.

© 2003 Acta Materialia Inc. Published by Elsevier Ltd. All rights reserved.

Keywords: Thermal barrier coating; Indentation; Columnar microstructure

1. Introduction

Thermal barrier systems used in gas turbines utilize various ternary oxides as the outermost insulating layer [1–3]. The prevalent oxide is yttria-stabilized-zirconia containing 7 wt% yttria (7YSZ). Newer materials for this application include gadolinium zirconate ($\text{Gd}_2\text{Zr}_2\text{O}_7$) [4], as well as zirconia with mixed rare earth stabilizers, such as gadolinia and yttria [5,6]. In principle, these materials are preferable to 7YSZ, because of their lower thermal conductivity. In practice, their durability is limited because of their susceptibility to erosion caused by sequential small particle impacts. One of the material properties affecting erosion durability is the plastic response at elevated temperature [7,8]. The plastic deformation is visually apparent in a cross section of a partially eroded material with a columnar

microstructure (Fig. 1) produced by electron beam physical vapor deposition (EB-PVD). Images of this type reveal a densified zone with associated plastic bending of some of the columns (Fig. 1). Shear bands, which are also apparent, become planes for preferential material removal during subsequent impacts [9].

Therefore, in order to assess the reliability and integrity of thermal barrier coatings at high temperature, its plastic behavior such as the hardness needs to be characterized. In this study, the spherical indentation test is adopted to measure the hardness and plastic response of the thermal barrier systems. A companion article describes a high temperature impression probe (Fig. 2(a)) for assessing the deformation resistance of actual EB-PVD layers and its application to a range of thermal barrier materials [9]. The probe is applicable to thermal barrier coatings with the columnar microstructures created by EB-PVD methods [2,3]. The loading system is rigid at high temperature (it uses sapphire for the substrate and the indenter), such that the measurements probe the deformation of the coating, only. The

* Corresponding author. Tel.: +1-212-854-3787; fax: +1-212-854-6267.

E-mail address: xichen@civil.columbia.edu (X. Chen).

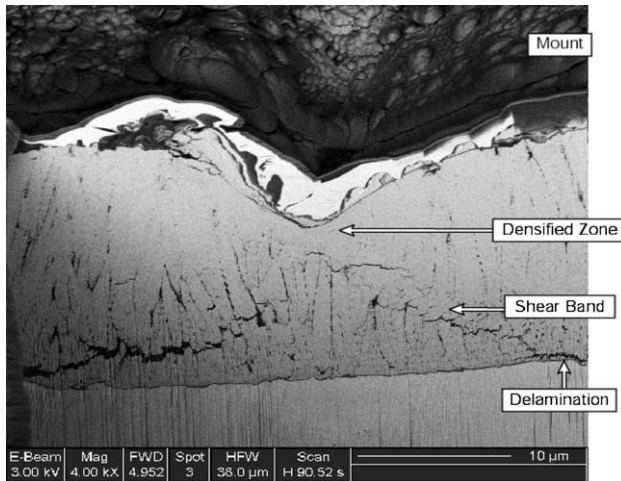


Fig. 1. A cross section of a 7YSZ material impacted at high temperature.

intent of this article is to perform simulations that allow de-convolution the flow stress, and other properties, as well as the plastic strain, from the load/deflection response of a quasi-static indentation experiment. Experimental and numerical characterization of dynamic impact on thermal barrier systems (also known as foreign object damage) have been addressed elsewhere [8].

Indentation measurements performed on homogeneous, isotropic bulk materials [10,11] can be used to extract the yield stress σ_Y and indentation modulus M using:

$$H = P/A = c_b \sigma_Y, \quad (1)$$

and

$$S = \beta \frac{2}{\sqrt{\pi}} M \sqrt{A}, \quad (2)$$

The hardness H is the ratio between indentation load P and projected contact area A . The initial unloading slope is denoted by S and $M = E/(1 - \nu^2)$, is the plane-strain modulus. In these formulae, the finite compliances of the measuring system and the indenter tip have been neglected. The yield strength and Poisson ratio of the bulk material are σ_Y and ν , respectively. The constant c_b is a constraint factor [12] that depends on indenter shape and material properties, and β is a shape factor ($\beta = 1$ for axi-symmetric indenters and $\beta = 1.03$ – 1.05 for indenters with square or rectangular cross-sections) [13]. For most bulk engineering materials $c_b \approx 3$, independent of the indentation depth [12,14].¹ These formulae cannot be applied to inhomogeneous coatings, such as columnar/porous TBCs, for several reasons. (a) The micro-

structure is compliant and anisotropic due to the gaps between the columns. (b) Inter-columnar friction must be addressed. (c) The impression depths can become large enough for the measurements to be affected by the properties of the substrate [14,15]. To incorporate these effects, the finite element method (FEM) is used. The method allows the material properties and microstructures to be varied over a wide range.

Basic experimental information obtained using this test is summarized on Fig. 3 [9]. Load/deflection curves measured at elevated temperature (1150 °C), summarized on Fig. 3(a), indicate differences in response between materials governed by their respective deformation resistance. Observations of cross sections (Fig. 3(b)) show a variety of deformation responses, including shear bands, with features comparable to those found after impact (Fig. 1). One objective of the simulations is to relate the incidence of these bands to the columnar microstructure of the material.

2. Model description

The axi-symmetric model for impression of the TBC, thickness h_{tbc} , is shown in Fig. 2(b). The indenter is a rigid sphere with radius R (250 μm in the experiments [9]). A load P is imposed, resulting in an impression of depth, δ , and contact radius, a . The columns are modeled as annuli around the center of symmetry. They are assumed to be straight and parallel before deformation, all having width d , with gap, w , between columns. The number of columns that can be included in the model is restricted by computational time. The following results include about 20–24 annular columns within the contact zone. In the experiments, the number of columns intersected within the plane of the contact is 50 (Fig. 3(b)), such that the actual number in contact with the indenter in the three-dimensional geometry is about 2000. This difference causes some of the foregoing results to be qualitative in nature, as elaborated below.

The material in the TBC columns is considered to be isotropic, with properties representative of porous zirconia. The base (non-porous) TBC material is considered to be elastic-perfectly plastic, with yield stress σ_Y , and governed by a Von Mises yield surface. Prior assessments indicate that the Poisson ratio, taken to be $\nu = 0.25$, should have minimal affect [16]. The initial porosity within each TBC column is considered to be, $f_0 = 0.1$, and the elastic-perfectly plastic Gurson model [17] is employed to represent the material. Coulomb friction is assumed at the contact with the indenter, μ_{contact} , and between columns, μ_{tbc} . Provided that the indentations are shallow such that the substrate effect is negligible [14], dimensional analysis dictates the following general relationship:

¹ For metals it is observed that the hardness increases with decreasing indentation depth, when the penetration is in the sub-micron regime generally believed due to strain gradient hardening. We ignore this effect for the TBC.

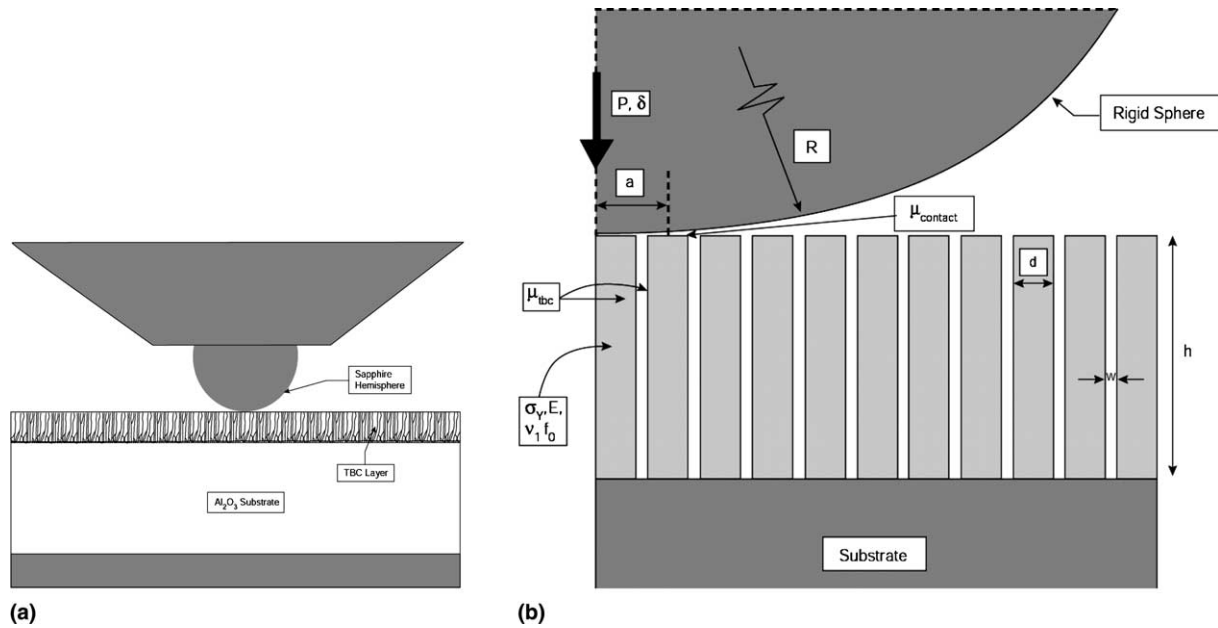


Fig. 2. (a) schematic of the test configuration which is inserted into a high temperature servo-hydraulic loading system [9] to impose the loads and measure the displacements. (b) Schematic showing of the axi-symmetric model for indentation of the TBC.

$$\frac{P}{\pi a^2 \sigma_Y} = F \left[\frac{\sigma_Y}{E}, \frac{\delta}{d}, \frac{d}{h}, \frac{w}{h}, \mu_{\text{contact}}, \mu_{\text{tbc}} \right], \quad (3)$$

where the initial porosity is understood to be fixed at $f_0 = 0.1$. Here, the strain hardening effect at the high temperature is ignored. The effects of friction and Poisson's ratio are also neglected since they play only minor role during indentation [14]. The contact is assumed to be frictionless and the Poisson's ratio is taken to be 0.25 for the TBC. To take advantage of the columnar microstructure, we further assume that the indentation does not cause any material pile-up or sink-in. Based on these assumptions, the normalized hardness can be sufficiently characterized by the dimensionless groups shown in (3). These parameter groups are then implemented in the finite element analysis.

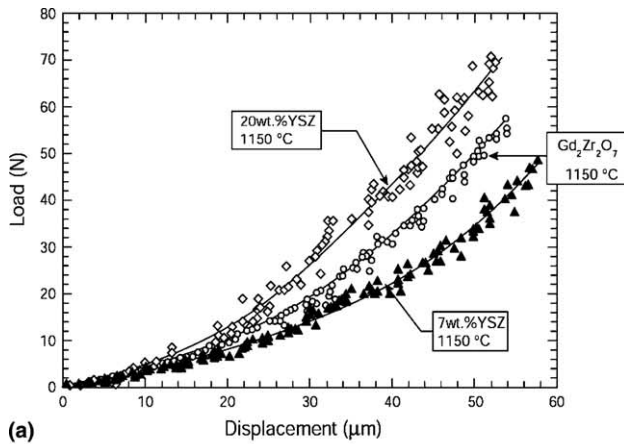
Finite element calculations were performed using the commercial code ABAQUS [18]. The option for finite deformation and strain was employed. A typical mesh comprises about 20 000 4-node axisymmetric elements with reduced integration. The projected contact area is calculated by analyzing the nodes in contact with the indenter. To obtain representative results, $d/h = 0.1$ and $\sigma_Y/E = 0.001$ are adopted in all cases. The primary emphasis concerns the effects of the column gap, w/d , and frictional conditions μ_{contact} , μ_{tbc} on the change in normalized hardness $\bar{H} \equiv P/\pi a^2 \sigma_Y$, as the penetration depth δ/d increases.

3. Sphere indentation

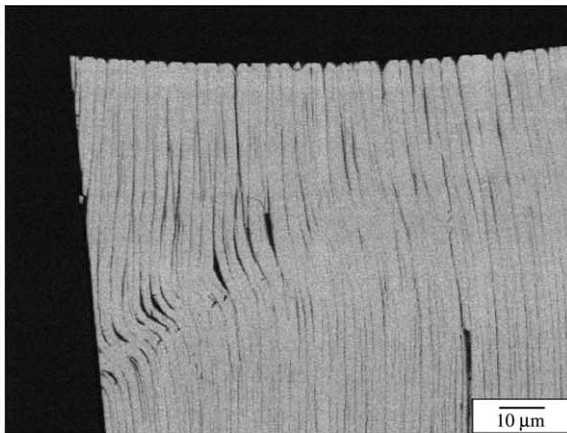
Loads and pressures have been computed for a range of frictional conditions at the contact, μ_{contact} , as well as

variations in the gap width and inter-columnar friction coefficient (Fig. 4). Consistent with prior assessments, there is essentially no effect of μ_{contact} (Fig. 4(a)). These curves are not smooth because of the discrete nature of the contact events. The influence of gap width (Fig. 4(b)) is shown for sticking friction between the columns ($\mu_{\text{tbc}} = 0.5$). Note that the indentation pressure increases with decreasing gap size. Moreover, as the penetration increases, more TBC columns contact and stick, causing the pressure to increase. At the deepest penetration, for the narrowest gap, the pressure approaches the limit of homogeneous material, $c_b \rightarrow 3$. The influence of inter-columnar friction is explored for a narrow gap, $w/d = 0.001$, using sticking contact ($\mu_{\text{tbc}} = 0.5$), sliding contact ($\mu_{\text{tbc}} = 0.1$), and frictionless contact ($\mu_{\text{tbc}} = 0$). The results are summarized on Fig. 4(c). When friction is absent, the load, $P/\pi a^2 \sigma_Y \approx 1.6$, is insensitive to penetration, δ/d (Fig. 4(c)). In this limit, the TBC is about 50% softer than its homogeneous counterpart. For finite inter-columnar friction, larger loads are needed to overcome the slip resistance, causing the hardness to increase both with penetration and with increase in μ_{tbc} . The same analyses reveal trends in the column deformation and densification with contact friction (Fig. 5). Stresses have been ascertained but these are not shown. Note that the columns bend *away* from the center of symmetry when the contact is *frictionless*, but *toward* the center for *sticking* friction. For finite, but small, friction coefficient ($\mu_{\text{contact}} = 0.1$), the columns remain almost straight, with a slight bending *toward* the center.

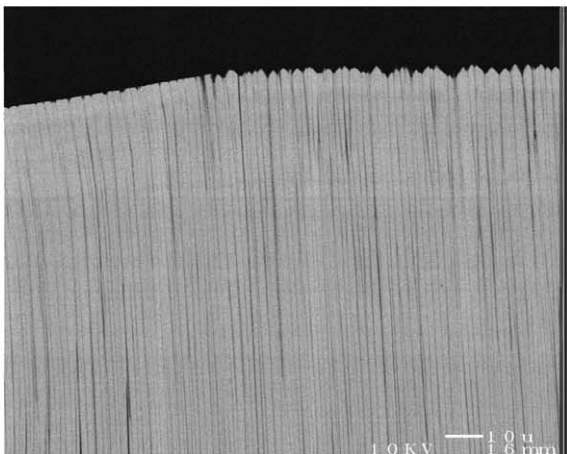
Superposing the experimental results obtained for 7YSZ at 1150 °C onto the theoretical results in Fig. 4(b) indicates one aspect of the protocol for using the



(a)



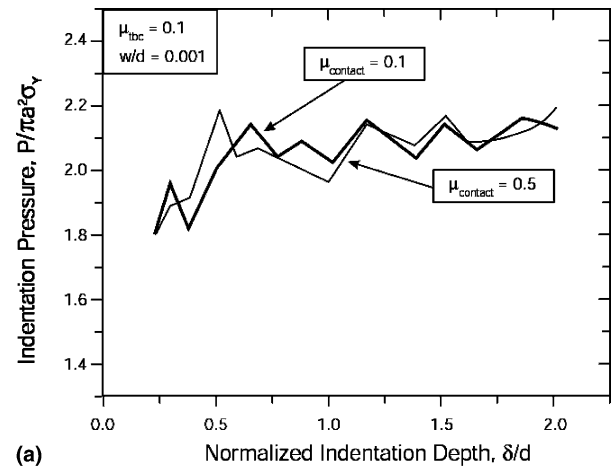
(b)



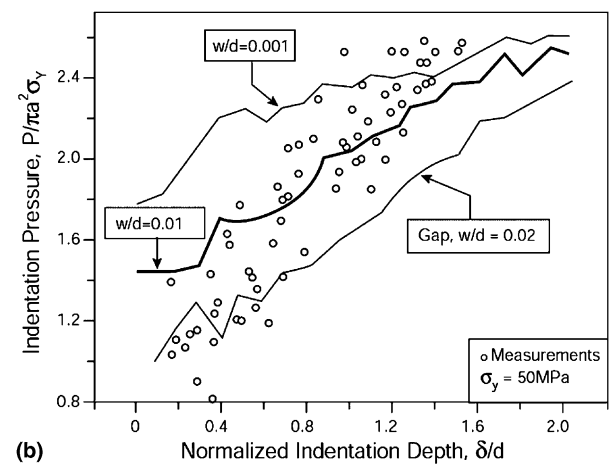
(c)

Fig. 3. (a) Load/deflection measurements obtained by impressing three different thermal barrier oxides at 1150 °C. (b) Scanning electron image of a polished cross section through the $Gd_2Zr_2O_7$ specimen impressed at 1150 °C. Note that the shear band forms beneath the center of contact and extends outward at an inclination of about 45°. Also note that the columns bend away from the center of symmetry. (c) Image of the same impression shown on Fig. 3b, highlighting the contact periphery to show the direction of the column bending.

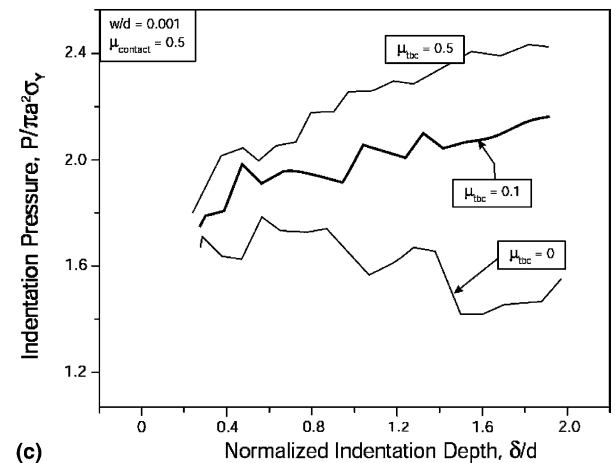
simulations to de-convolute the measurements. A best fit is obtained by using the unknown yield strength as a parameter. This procedure reveals yield strength, $\sigma_y \approx 50$ MPa [9]. The method does not appear to be



(a)



(b)



(c)

Fig. 4. Indentation pressure $P/(\pi a^2 \sigma_y)$ as a function of normalized indentation depth δ/d presented for different microstructures: (a) The effect of contact friction, with $\mu_{\text{contact}} = 0.1$ and 0.5 ; (b) The effect of gap sizes for three representative gap width, $w/d = 0.001, 0.01$ and 0.02 ; the experimental results obtained for 7YSZ at 1150 °C are also shown; (c) The effect of inter-columnar friction, with $\mu_{\text{tbc}} = 0, 0.1$ and 0.5 .

discriminating with regard to gap width, but the relatively large positive slope, $d\bar{H}/d(\delta/d)$, associated with the measurements seems to exclude the possibility that the columns are frictionless. Ascertaining the actual

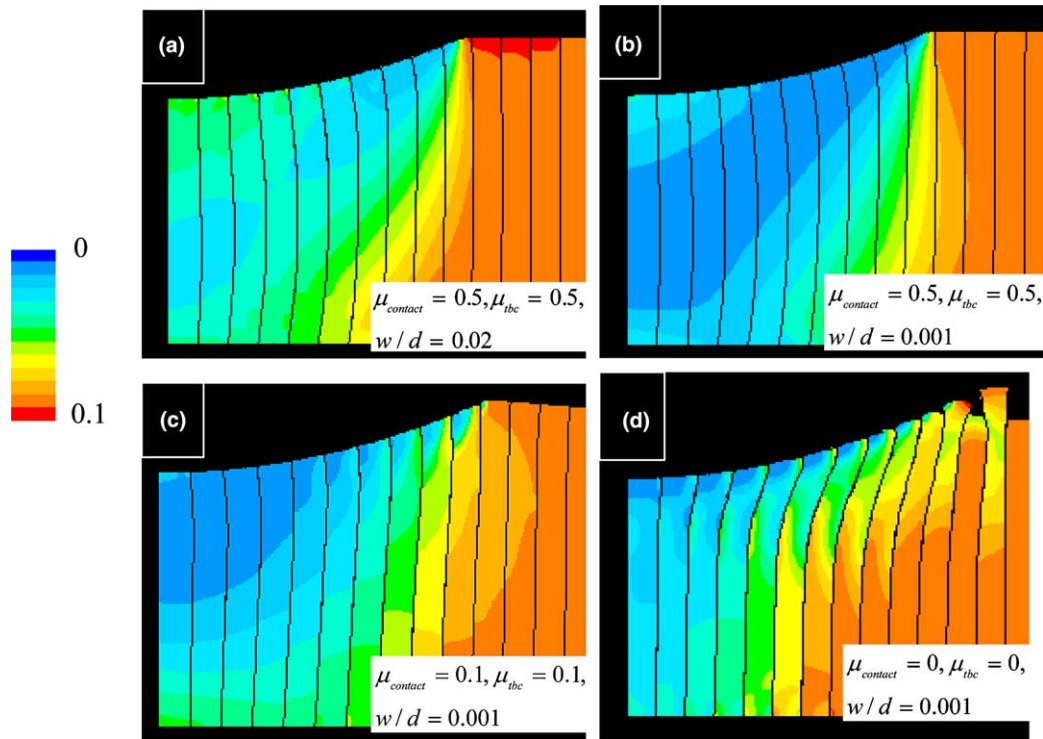


Fig. 5. Trends in the column deformation and densification (color coded) with various contact friction and inter-columnar friction conditions. Note that the characteristics of column bending are very sensitive to the contact friction.

value of the friction coefficient, μ_{tbc} does not appear realistic, because the relatively small number of columns used in the calculations would underestimate the influence of friction. Additional insights about inter-columnar friction emerge in the next section.

The sign of the column bending observed experimentally (Fig. 3(c)) allows $\mu_{contact}$ to be ascertained, using the column boundaries as fiducial markers. *The concept is comparable to the use of embedded, sub-surface grids to evaluate plastic deformation* [12]. The observed bending (Fig. 3(c)) is inconsistent with a frictionless contact (Fig. 5(d)). It also appears to be inconsistent with sticking friction (Figs. 5(a) and (b)). The best match between the calculations and observations occurs for a finite, small friction coefficient, $\mu_{contact} \approx 0.1$ (Fig. 5(c)). This relatively low friction might be attributed to the fact that the column tips flatten in order to conform to the shape of the indenter [9]. Note that friction coefficients in the range, $\mu_{contact} \approx 0.1$, are consistent with prior assessments of related indentation contact problems [12,16].

4. Shear bands

The axisymmetric model appears to be too constrained to reveal the occurrence of shear bands. A plane strain model subject to flat (punch) indentation is more

amenable to investigation of the deformation heterogeneities (Fig. 6). Preliminary calculations of this type indicated that heterogeneous deformations resembling the experimentally observed bands (Fig. 3(b)) only arise when both of the friction coefficients (μ_{tbc} and $\mu_{contact}$) are finite, but relatively small. They do not arise either for frictionless interfaces or for sticking friction. A synopsis of the results revealing heterogeneous deformation is presented on Fig. 6(a) and (b), focusing on the column shapes rather than the stresses (for variety, Fig. 6(a) plots the shear stress and Fig. 6(b) plots the Mises stress). For friction coefficients, $\mu_{tbc} \approx 0.2$ and $\mu_{contact} \approx 0.1$, and a yield strength representative of 7YSZ at 1150 °C ($\sigma_Y \approx 50$ MPa), the deformation pattern that develops in the columns (Fig. 6(a)) is comparable to that observed in the experiments (Fig. 3(b)). Note that gaps between the columns that occur in the region of the band are synonymous with the gaps found experimentally. Upon using a much higher yield strength ($\sigma_Y \approx 4$ GPa), representative of these materials at much lower temperature, the shear band seems to extend in the opposite sense (Fig. 6(b)), originating at the contact periphery. This orientation has not been observed experimentally.

The conclusion to be drawn from this assessment is that the susceptibility of the columnar microstructure to shear bands is contingent on the nature of both the contact and inter-columnar friction, requiring finite but

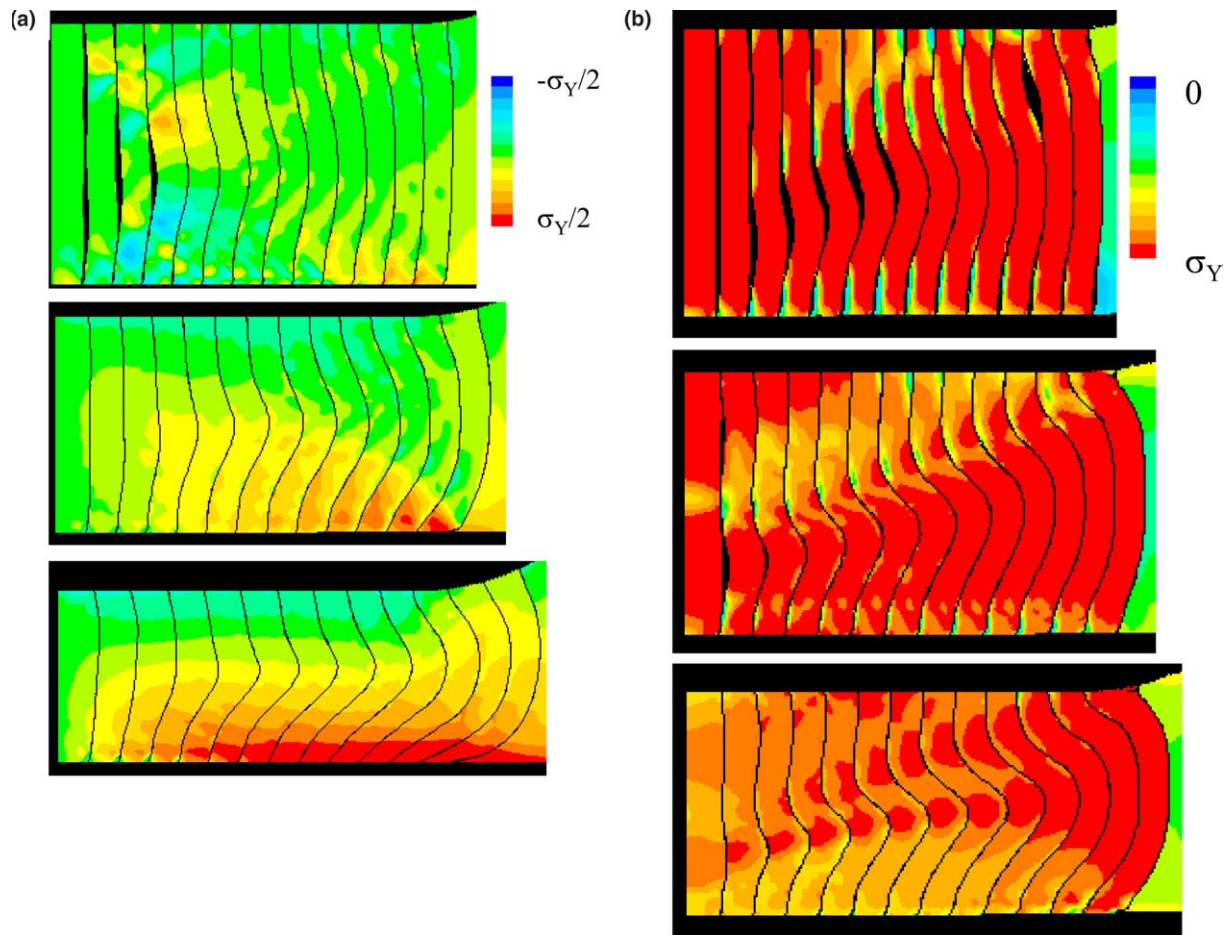


Fig. 6. (a) Sequential contour plots of the shear stress in TBC columns under flat indentation, with $w_d = 0.1$, $\mu_{\text{contact}} = 0.05$ and $\mu_{\text{tbc}} = 0.2$. Notice the occurrence of shear bands. (b) Sequential contour plots of the Mises stress in TBC columns under flat indentation, with $w_d = 0.1$, $\mu_{\text{contact}} = 0.1$ and $\mu_{\text{tbc}} = 0.1$. The shear bands develop when both μ_{contact} and μ_{tbc} are finite but relatively small.

small friction coefficients. Additional studies are needed to reveal the details.

5. Conclusion

Calculations have been performed that allow interpretation of results obtained using a high temperature probe applicable to thermal barrier oxides with a columnar microstructure. The variables in the calculations include the contact friction, μ_{contact} , the inter-columnar friction, μ_{tbc} , the width of the gaps between the columns, w , and the yield strength of the base material of the TBC columns, σ_Y .

The indentation pressure (normalized by the yield strength, \bar{H}), when calculated as a function of the impression depth, indicates constraint factors insensitive to μ_{contact} , but dependent on μ_{tbc} and w . It is shown that comparisons with measurements [9] allow determination of σ_Y and provide estimates of μ_{tbc} . At 1150 °C, $\sigma_Y \approx 50$ MPa was inferred for the base material. Given 10% initial porosity, the yield strength of the porous material

is about 45 MPa. The calculations reveal the bending of the columns within the impression zone as a function of μ_{contact} . The columnar boundaries act as internal fiducial lines such that, upon comparison with observations, the contact friction has been assessed as $\mu_{\text{contact}} \approx 0.1$.

Plane strain calculations have been used to gain some insight into the conditions that allow shear bands to form in columnar systems. These show, qualitatively, that relatively low friction coefficients (μ_{contact} and μ_{tbc}), in conjunction with high yield strength, σ_Y , favor the heterogeneous deformations. Additional studies are needed to reach quantitative conclusions. Given their importance to material removal by particle impact, studies of shear banding will continue.

References

- [1] Miller RA. Thermal Barrier Coatings for Aircraft Engines – History and Directions. Thermal Barrier Coating Workshop (NASA Conference Publication 3312). Cleveland, OH: NASA, 1995.

- [2] Evans AG, Mumm DR, Hutchinson JW, Meier GH, Pettit FS. *Prog Mater Sci* 2001;46:505.
- [3] Stiger MJ, Yanar NM, Pettit FS, Meier GH. Mechanisms for the failure of electron beam physical vapor deposited thermal barrier coatings induced by high temperature oxidation. In: Hampikian JM, Dahotre NB, editors. *Elevated temperature coatings: science and technology III*. Warrendale (PA): The Minerals Metals and Materials Society; 1999. p. 51.
- [4] Maloney MJ. Thermal barrier coating systems and materials. In: U.S. Patent 6,177,200. Hartford (CT): United Technologies Corporation, 2001.
- [5] Nicholls JR, Lawson KJ, Johnstone A, Rickerby DS. *Surf Coat Tech* 2002;151–152:383.
- [6] Zhu D, Miller RA. *Ceram Eng Sci Proc* 2002;23:457.
- [7] Bruce RW. *Tribol T* 1998;4:399.
- [8] Chen X, Wang R, Yao N, Evans AG, Hutchinson JW, Bruce RW. *Mater Sci Eng* 2003;A352:221.
- [9] Watanabe M, Mercer C, Levi CG, Evans AG. *Acta Materialia*, submitted.
- [10] Doerner MF, Nix WD. *J Mater Res* 1986;1:601.
- [11] Oliver WC, Pharr GM. *J Mater Res* 1992;7:1564.
- [12] Johnson KL. *Contact mechanics*. Cambridge: Cambridge University Press; 1985.
- [13] King RB. *Int J Solids Struct* 1987;23:1657.
- [14] Chen X, Vlassak JJ. *J Mater Res* 2001;16:2974.
- [15] ASTM. *Standard Test Method for Vickers Hardness of Metallic Materials*. ASTM, 1987.
- [16] Mesarovic SD, Fleck NA. *Proc R Soc Lond* 1999;455:2707.
- [17] Gurson AL. *J Eng Mater Tech* 1977;99:2.
- [18] Hibbit, Karlsson & Sorensen Inc. *ABAQUS version 5.7 User's Manual*, Pawtucket (RI): Hibbit, Karlsson & Sorensen Inc., 1998.